RandP: Effective and Efficient Medical Visual In-Context Learning via a Retrieve-and-Propagate Module for Prompt-Query Fusion

Rongge Mao[1,2] RONGGEMAO@MAIL.USTC.EDU.CN
[1] *School of Biomedical Engineering, Division of Life Sciences and Medicine, University of Science and Technology of China (USTC), Hefei, 230026, China*
[2] *Center for Medical Imaging, Robotics, Analytic Computing & Learning (MIRACLE), Suzhou Institute for Advance Research, USTC, Suzhou, 215123, China*
Han Li[3] TUM_HAN.LI@TUM.DE
[3] *Computer Aided Medical Procedures (CAMP), Technische Universitaet Muenchen (TUM).*
Chengqi Dong[1,2] DONGCQ@MAIL.USTC.EDU.CN
Nassir Navab[3] NASSIR.NAVAB@TUM.DE
S.Kevin Zhou[*1,2,4,5,6] SKEVINZHOU@USTC.EDU.CN
[4] *Key Laboratory of Intelligent Information Processing of Chinese Academy of Sciences (CAS), Institute of Computing Technology, CAS, Beijing, 100190, China*
[5] *Jiangsu Provincial Key Laboratory of Multimodal Digital Twin Technology, Suzhou, 215123, China*
[6] *State Key Laboratory of Precision & Intelligent Chemistry, USTC, Hefei, China ORCID (S.Kevin Zhou): https://orcid.org/0000-0002-6881-4444*

Editors: Under Review for MIDL 2026

Abstract

Visual In-Context Learning (ICL) has emerged as a promising paradigm for constructing vision generalists by conditioning on prompt pairs. Existing visual ICL methods typically adopt a grid-like prompt-query construction combined with Masked Image Modeling (MIM) as the training strategy. However, directly applying these frameworks to medical imaging tasks often leads to suboptimal performance. Moreover, the reliance on MIM restricts the backbone to Vision Transformer (ViT) and introduces unnecessary computational overhead due to the need to reconstruct the prompt label. In this work, we revisit previous visual ICL paradigms for medical imaging and propose a training-inference aligned masking strategy to replace MIM. We further introduce a Retrieve-and-Propagate (RandP) module to enhance prompt-query fusion under this masking scheme. Experimental results show that our RandP visual ICL framework not only doubles the inference speed compared to prior visual ICL baselines but also achieves superior performance across multiple medical imaging tasks. Furthermore, unlike previous approaches constrained to vanilla ViT, our framework is compatible with U-Net-style architectures, enabling broader applicability and improved effectiveness in the medical imaging domain. Our code will be available after the paper is accepted.

Keywords: Medical imaging, Visual In-Context-Learning.

* Corresponding Author

1. Introduction

Accurate medical image analysis is crucial for diagnosing various diseases (Zhou et al., 2021). With the advancement of deep learning techniques, many tasks in medical image analysis, such as classification (Yue and Li, 2024), detection (Li et al., 2022a), segmentation (Ronneberger et al., 2015), restoration (Yang et al., 2024), reconstruction (Wang et al., 2019), registration (Balakrishnan et al., 2019) and report generation (Wu et al., 2022), have made substantial progress. However, most studies concentrate on specific visual tasks, anatomical regions, and image modalities, developing specialized network architectures, training methods, and techniques tailored to these tasks. Consequently, these models often lack generalizability across different medical imaging tasks.

Recent research has also demonstrated the efficacy of ICL in vision-language tasks (Zhou et al., 2024). In the medical domain, GPT-4V (OpenAI et al., 2024) has achieved impressive results: using few-shot in-context learning, it has matched or even surpassed the performance of expert-designed convolutional neural networks (CNNs) on various pathology classification tasks, such as colorectal tissue typing, polyp subtype identification, and lymph node metastasis detection, with as few as 1–10 exemplars (Ferber et al., 2024). Comparable success has been observed in COVID-19 chest X-ray classification and tauopathy recognition tasks (Chen et al., 2023). These findings underscore GPT-4V's capabilities in one-shot generalization, interpretability, and reduced annotation burden in biomedical imaging (Wu et al., 2023). However, these methods focus on sparse prediction tasks (e.g., classification, Visual Question Answering), rather than dense prediction tasks (e.g., segmentation, denoising).

Given the demonstrated effectiveness of ICL in both natural language processing (NLP) and vision-language domains for sparse prediction tasks, a natural and compelling question arises: **Can the in-context learning paradigm be effectively extended to dense prediction tasks in computer vision, particularly in the field of medical imaging?**

In the field of natural images, the answer is yes. Pioneering studies have explored visual In-Context Learning (vICL) for dense prediction tasks and achieved encouraging results. For instance, MAE-VQGAN (Bar et al., 2022) formulates vICL as an image inpainting task by concatenating prompt-query pairs and employing a random masking strategy (He et al., 2022) to predict the discrete visual tokens (Esser et al., 2021) corresponding to the masked patches. This framework enables the model to perform various visual tasks by conditioning on different prompts. Similarly, Painter (Wang et al., 2023) adopts a simpler Masked Image Modeling (MIM) approach (Xie et al., 2022), directly regressing pixel values in the image space. MVG (Ren et al., 2024) extends Painter to the medical imaging domain, adopting a hybrid training scheme that combines autoregressive training with MIM. However, the distinct properties of medical images limit the effectiveness of directly adopting natural image vICL methods, revealing a critical yet underexplored need for domain-specific frameworks.

In this study, we identify key limitations of existing visual in-context learning models in medical imaging, such as **ineffective masking strategies, rigid backbone, and high computational overhead.** To address these challenges, we adopt a novel training-inference aligned masking strategy along with a Retrieve-and-Propagate (RandP) module, both of which enhance prompt-query interaction and simultaneously reduce the number

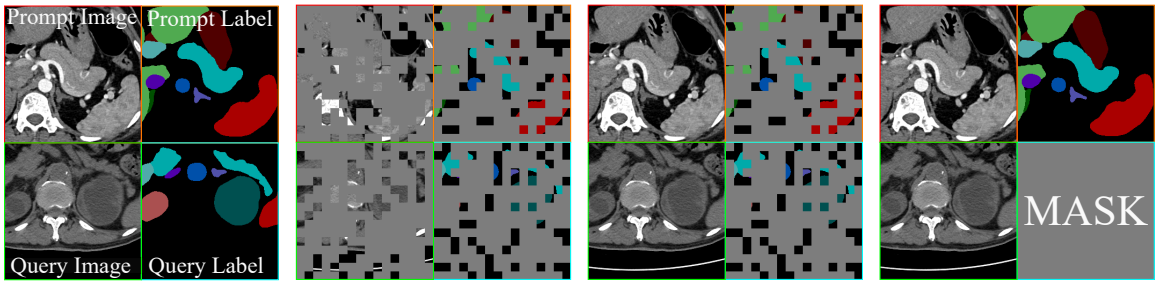

(a) Grid-like Image (b) MAE-VQGAN (c) Painter (d) Ours

Figure 1: Illustration of different visual ICL mask strategies during training. Gray patches indicate masked areas.

of visual tokens, which in turn improves model efficiency and performance. Unlike prior MIM-based vICL methods that are tied with ViT backbone, our framework generalizes to convolutional networks and other non-transformer designs, enabling broader applicability to dense prediction vision generalist in medical imaging. **Our main contributions are as follows**:

1. Comprehensive Analysis of Existing vICL Frameworks. We present a comprehensive analysis of the limitations of current vICL frameworks in medical imaging, regarding masking design, backbone flexibility and efficiency.

2. Training–Inference Aligned vICL with Retrieve-and-Propagate Module. We propose a medical vICL framework adopting a training-inference aligned masking strategy and a Retrieve-and-Propagate module to improve performance and computational efficiency.

3. Enabling vICL for U-Net–style Architectures. Our experiments demonstrate that our framework can be effectively extended to U-Net-style models (Ronneberger et al., 2015), which was not feasible for prior vICL frameworks.

2. Limitations of Previous Visual ICL Methods in Medical Imaging

Recent advances (Bar et al., 2022; Wang et al., 2023; Liu et al., 2024; Bai et al., 2024) in vICL have demonstrated strong performance across a range of vision tasks. Despite these innovations, directly applying such approaches to medical imaging remains suboptimal due to the following key limitations:

(i) Ineffectiveness of MIM in Medical Settings. Naive masked image modeling typically involves randomly masking a large portion (e.g., 75%) of the input image. However, in medical imaging scenarios, where images often contain large homogeneous background regions, this approach fails to preserve sufficient task-relevant information for effective prompt-query reasoning. Furthermore, as illustrated in Fig.1.(a) and Fig.1.(c), the masking strategies shown are those adopted during the training phase of MIM-based visual ICL models. In contrast, the inference stage requires the use of a different masking strategy, as depicted in Fig.1.(d). This inconsistency results in a discrepancy between the training and inference procedures, which introduces **a gap between training and inference**.

Table 1: Comparison of the segmentation performance, measured by the Dice Similarity Coefficient (DSC, in percentage), using different inference strategies.

	MAE-VQGAN	PromptGIP	Painter
Standard Inference	**44.14**	**69.92**	**78.99**
Training-like Inference	83.20	88.64	86.43
Modified Inference	1.88	49.09	23.09

To further investigate this issue, we carefully design three distinct inference strategies for the trained vICL models MAE-VQGAN, Painter, and PromptGIP (Liu et al., 2024):

1.Standard Inference: The typical vICL setup where the prompt image, prompt label, and query image are fully visible, and only the query label is fully masked (100%).

2.Training-like Inference: Matches the training phase masking strategy, providing partial visibility to the query label during inference.

3.Modified Inference: Replaces the partially visible query label patches with black patches before applying Training-like Inference.

Under the **Training-like Inference** setting, a small portion of the ground truth (GT) is exposed to the model. Therefore, evaluation metrics are computed only on the masked patches, without the visible GT regions to ensure a fair assessment. From Table 1, we observe that all models achieve their highest performance under the *Training-like Inference* setting. However, this setting grants the model partial access to the GT which is unrealistic in practical scenarios. When even this limited GT is removed, as in the **Modified Inference** setting, the performance drops sharply (e.g., MAE-VQGAN: 83.20% $\rightarrow$ 1.88%). These results indicate that visual ICL models trained via MIM are primarily effective at inpainting, meaning they infer missing content based on visible patches, rather than truly understanding and interpreting the query image. However, this capability is misaligned with the requirements of medical visual tasks, which demand a comprehensive understanding of the query image itself.

Moreover, comparing **Standard Inference** and **Modified Inference**, their main difference lies in whether the prompt labels are provided in full or only partially. When the prompt labels are reduced from complete to partial, model performance also declines significantly(e.g., Painter: 78.99% $\rightarrow$ 23.09%). This further underscores that prompts play a crucial role in guiding the model's processing of the query image within the vICL framework.

(ii) Unnecessarily High Computational Overhead. Although models like Painter and MVG attempt to mitigate this issue by adding image and label patches at shallow layers, **they still devote nearly half of their computational budget to prompt processing**. This allocation limits the model's capacity to focus on the query task itself, reducing overall efficiency.

(iii) Limited Backbone Flexibility. MIM-based methods are tightly coupled with transformer-based architectures (Vaswani et al., 2023) and often perform poorly on convolutional networks (Tian et al., 2023), limiting their compatibility with widely used backbones in medical image analysis, such as U-Net (Ronneberger et al., 2015) and its variants, which are more suitable for image-to-image tasks in medical imaging.

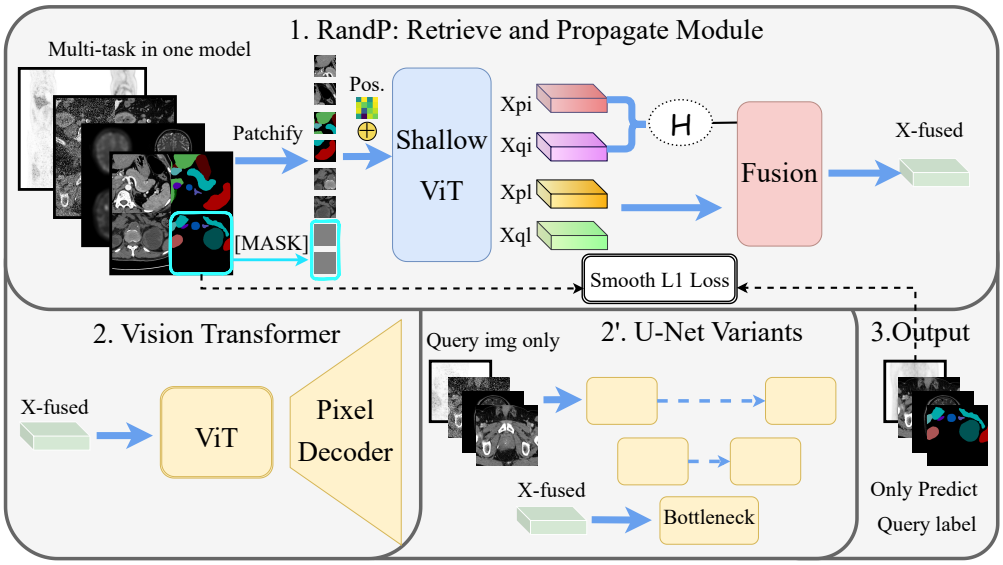

Figure 2: The grid-like image is first processed by the Retrieve-and-Propagate (RandP) Module (1) to produce *X-fused* feature, which can be fed into either a ViT backbone (2) with a pixel decoder or a U-Net-style (2') architecture to get the dense output. The query label is replaced with [MASK] tokens, which then serves as the Ground Truth to calculate the loss against the output. The italicized pi, pl, qi, and ql denote the prompt image, prompt label, query image, and query label, respectively. H denotes Hungarian matching (Kuhn, 1955), and *Pos.* stands for positional encoding (Vaswani et al., 2023).

3. Method

RandP Framework. Our RandP medical vICL framework, as illustrated in the Fig.2, consists of three main components: a Retrieval-and- Propagate module for prompt-query fusion, a backbone for image feature extraction, and a pixel decoder for dense prediction.

Unifying Input and Output Spaces. For each *query image* in the training set, we randomly select another image with the same task and its corresponding label as the *prompt image* and *prompt label*. All four components—*prompt image*, *prompt label*, *query image*, and *query label*—are in $\mathbb{R}^{3\times H\times W}$. These are arranged into a grid: top-left, top-right, bottom-left, and bottom-right, respectively, forming a grid-like image $X \in \mathbb{R}^{3\times 2H\times 2W}$, as shown in Fig.1.(a). For segmentation tasks, which need to predict discrete one-hot labels, we follow (Wang et al., 2023) by assigning each semantic category a unique RGB color. During inference, the predicted label is obtained by mapping each output pixel to the nearest category via L_2 distance, effectively turning segmentation into an image-to-image translation task. For low-level tasks, where outputs are already continuous in RGB space, no such transformation is needed. After training, a given prompt image and label pair instructs the model to perform which task on the query image.

Training-Inference Aligned Masking Strategy. Unlike prior vICL approaches that predominantly rely on masked image modeling during training, we adopt a fully training-

inference aligned masking strategy, as depicted in Fig.1.(d). In our setting, the *prompt image*, *prompt label*, and *query image* are never masked, while the *query label* is always fully masked. This design offers several advantages:

1. **Consistency between training and inference:** By avoiding partial masking of the query image, the model is encouraged to truly understand the query image rather than simply reconstructing grid-like masked patterns, thus improving generalization to real ICL scenarios.

2. **Broader backbone compatibility:** This strategy allows the use of backbones beyond ViT. Prior work (Tian et al., 2023) has shown that the effectiveness of naive MIM degrades on CNNs due to the sparsity of masked inputs being diluted through stacked convolutional layers. By eliminating MIM-style masking, our framework can more effectively utilize convolutional architectures.

3. **Reduced computational cost:** Since the prompt label is never masked, there is no need to reconstruct it. Consequently, the model only needs to predict the query label, enabling us to discard prompt-related tokens after the prompt information has been integrated. This leads to significant computational savings without compromising performance.

Retrieval-and-Propagate Module for Prompt-Query Fusion. In previous vICL methods, prompt tokens and query tokens are concatenated into a single sequence and interact via self-attention. However, due to the quadratic complexity $\mathcal{O}(N^2)$ of self-attention with respect to sequence length, this design introduces considerable computational overhead compared to conventional image-to-image models that do not use prompts.

While the redundancy of visual tokens has been extensively validated in MLLMs (Chen et al., 2024), we argue that a similar level of redundancy may exist even when visual tokens are used purely as context. Inspired by recent efforts on visual token pruning or merging in MLLMs (Bolya et al., 2023; Zhang et al., 2025b; Wen et al., 2025), we propose to fuse prompt and query tokens at the early stage of the network to reduce computation and enhance efficiency.

We introduce a **Retrieval-and-Propagate** token fusion strategy, which is particularly inspired by the characteristics of medical images from different patients tend to exhibit strong visual similarities within corresponding anatomical regions—often more pronounced than those observed in natural images. Specifically, let $\mathbf{I}_{pi}$, $\mathbf{I}_{pl}$, $\mathbf{I}_{qi}$, and $\mathbf{I}_{ql}$ denote the prompt image, prompt label, query image, and query label, respectively. These inputs are first embedded with a patch embedding layer and added with learnable positional encodings:

$$\mathbf{Z}_{pi},\ \mathbf{Z}_{pl},\ \mathbf{Z}_{qi} = \text{PatchEmbed}(\mathbf{I}_{pi},\ \mathbf{I}_{pl},\ \mathbf{I}_{qi}) + \mathbf{P} \tag{1}$$

The resulting latent representations are then fed into a shallow ViT encoder (e.g., 2 layers) to extract features:

$$\mathbf{X}_{\text{pi}},\ \mathbf{X}_{\text{pl}},\ \mathbf{X}_{\text{qi}},\ \mathbf{X}_{\text{ql}} = \text{ViT}([\mathbf{Z}_{\text{pi}},\ \mathbf{Z}_{\text{pl}},\ \mathbf{Z}_{\text{qi}},\ [\text{MASK}]]) \tag{2}$$

Here, $\mathbf{Z}_*$ and $\mathbf{X}_*$ represent the latent representations before and after the encoder, respectively; $\mathbf{P}$ denotes the positional encoding. [MASK] is the learnable *mask token* used to replace the masked query label.

For each patch in the query image, we compute its cosine similarity with all patches in the prompt image, effectively allowing each query token to **Retrieve** similar token from the prompt.

To preserve the full information of the prompt pairs, we employ Hungarian matching (Kuhn, 1955) rather than greedy matching, as it enforces globally optimal one-to-one correspondences between query and prompt tokens based on the similarity matrix:

$$\mathcal{M} = \text{Hungarian}\left(-\text{Norm}(\mathbf{Z}_{\text{pi}}) \cdot \text{Norm}(\mathbf{Z}_{\text{qi}})^{\top}\right) \tag{3}$$

This design avoids information loss and ensures that each prompt token is effectively utilized in the fusion process. The matched prompt and query tokens are concatenated along the feature dimension and subsequently fused via a linear layer. If a highly similar prompt token is retrieved, the model can directly reuse the associated prompt label token, effectively **Propagating** it to the output.

$$\mathbf{X} = \text{Linear}\left(\text{Concat}\left[\mathcal{M}(\mathbf{X}_{\text{pi}}),\ \mathcal{M}(\mathbf{X}_{\text{pl}}),\ \mathbf{X}_{\text{qi}},\ \mathbf{X}_{\text{ql}}\right]\right) \tag{4}$$

Backbone and Pixel Decoder. Similar to previous visual ICL frameworks, we use ViT as the backbone. The pixel decoder is a simple prediction head with two convolutional layers, taking the concatenated feature maps from four different layers of ViT as input (Li et al., 2022b).

Loss Function. The decoder outputs an image in $\mathbb{R}^{3\times H\times W}$, and we compute the smooth L1 loss (Girshick, 2015) pixel-wise against the query label. Additionally, we use cross-entropy (CE) loss to optimize task prediction. The total loss function is as follows:

$$\mathcal{L} = \mathcal{L}_{\text{smoothL1}}(y_{\text{query\_label}}, \hat{y}_{\text{query\_label}}) + 0.1 \cdot \mathcal{L}_{\text{CE}}(y_{\text{task}}, \hat{y}_{\text{task}})$$

Extending Visual ICL via RandP + U-Net Variants Our masking strategy and RandP module enable the extension of visual ICL method to other non-transformer architectures, including the commonly used U-Net and its variants in medical imaging. Specifically, the activations output from the RandP Module, with a stride of 16, match the spatial dimensions of the feature maps after downsampling four times in U-Net. We adjust the channel dimensions of these activations using a 1×1 convolutional layer and add them element-wise to the feature maps in the U-Net bottleneck.

4. Experiment

Dataset and Implementation. Following (Yang et al., 2024), we select the IXI (LLC, 2024) MRI dataset for the super-resolution task, the 2016 NIH AAPM-Mayo Clinic Low-Dose CT Grand Challenge (McCollough et al., 2017) dataset for denoising task, and PET synthesis dataset provided by (Yang et al., 2024). Our segmentation dataset covers both CT and MRI modalities: PROMISE12 (Litjens et al., 2014), Prostate_MRI_Dataset (Ye et al., 2023), AMOS (Ji et al., 2022), and BTCV (Landman et al., 2015). Although we have chosen only these four tasks, our framework can be applied to any image-to-image task.

For all models, the shallow ViT encoder in the RandP Module uses two layers. We train for 100 epochs with a maximum learning rate of 1e−3, a batch size of 64, and a

Table 2: Performance comparison across different visual ICL frameworks. Inference metrics include FLOPs, runtime (per image on a RTX 3090), and memory usage (batch size = 16).

Models	Seg.	Denoising		Super-Res.		PET synthesis		FLOPs	Time	Mem.
	Dice	PSNR	SSIM	PSNR	SSIM	PSNR	SSIM	(G)↓	(ms)↓	(GB)↓
Copy	0.90	9.17	21.92	16.04	48.65	19.67	68.65	-	-	-
MAE-VQGAN	44.14	21.16	74.14	23.23	75.89	27.65	83.66	664	33.2	20.5
PromptGIP	69.92	31.1	90.18	28.36	88.29	27.77	86.26	670	33.1	18.8
Painter	78.99	32.83	91.94	30.11	**91.35**	31.16	89.75	429	30.6	15.5
MVG	82.56	32.97	92.08	30.11	91.34	31.09	89.85	429	30.5	15.6
RandP	**84.95**	**33.01**	**92.14**	**30.14**	91.33	**31.46**	**90.17**	**258**	**14.4**	**10.7**

Grid-like Image resolution of 512×512. In this paper, the reported DiceR (Dice, 1945) and SSIMR (Wang et al., 2004) values are presented in percentage form.

Comparison of Different Visual ICL Frameworks. We re-implement multiple prior vICL methods on our medical datasets, including MAE-VQGAN, PromptGIP, Painter, and MVG, to construct strong baselines for comparison. Additionally, we include AMIR (Yang et al., 2024), a router-based multi-task model in medical imaging. We also introduce a Copy baseline, which simply replicates the prompt label as the final output.For MAE-VQGAN, a pretrained VQGAN (Esser et al., 2021) is required to serve as the tokenizer. We initialized the VQGAN with weights pretrained on ImageNet (Deng et al., 2009) and further fine-tuned it on our datasets. In contrast, all other models perform regression directly in the pixel space. All frameworks adopt ViT as the backbone. As shown in Table 2, our proposed **RandP** framework consistently outperforms previous vICL frameworks across various tasks, while achieving **inference speed 2× faster** than prior visual ICL frameworks and **lower memory consumption**.

Table 3: Performance comparison under the Single-Task Separate Training Setting.

Models	Seg.	Denoising		Super-Resolution		PET synthesis	
	Dice	PSNR	SSIM	PSNR	SSIM	PSNR	SSIM
AMIR (Yang et al., 2024)	84.45	33.71	92.47	30.52	92.11	**31.56**	**90.48**
MVG (Ren et al., 2024)	77.91	32.54	91.65	29.94	91.08	31.19	89.96
RandP	79.32	32.80	91.88	29.93	91.17	31.18	89.97
RandP-UX-NET	83.27	32.77	89.82	29.44	91.02	30.40	88.72
RandP-SwinUNETR	83.63	32.44	89.33	29.16	90.25	30.67	89.13
RandP-Restormer	**84.89**	**33.73**	**92.58**	**30.54**	**92.27**	31.21	90.14

Table 4: Performance comparison under the Multi-Task Joint Training Setting. Values in parentheses indicate the performance gain compared to single-task training. UX., Sw., and Res. refer to UX-NET, SwinUNETR, and Restormer, respectively.

Models	Segment.	Denoising		Super-Resolution		PET synthesis	
	Dice	PSNR	SSIM	PSNR	SSIM	PSNR	SSIM
AMIR	83.5(-0.9)	33.9(+0.2)	92.8(+0.3)	30.8(+0.3)	92.3(+0.2)	31.6(+0.1)	90.6(+0.1)
RandP	85.0(+5.6)	33.0(+0.2)	92.1(+0.2)	30.1(+0.2)	91.3(+0.2)	31.5(+0.3)	90.2(+0.2)
RandP-UX.	84.1(+0.8)	33.8(+1.0)	92.7(+2.9)	30.5(+1.0)	92.0(+1.0)	31.6(+1.2)	90.4(+1.6)
RandP-Sw.	84.2(+0.6)	33.7(+1.3)	92.6(+3.3)	30.3(+1.1)	91.6(+1.4)	31.6(+0.9)	90.3(+1.1)
RandP-Res.	85.7(+0.8)	34.0(+0.3)	92.9(+0.3)	30.8(+0.3)	92.5(+0.2)	32.1(+0.9)	91.0(+0.9)

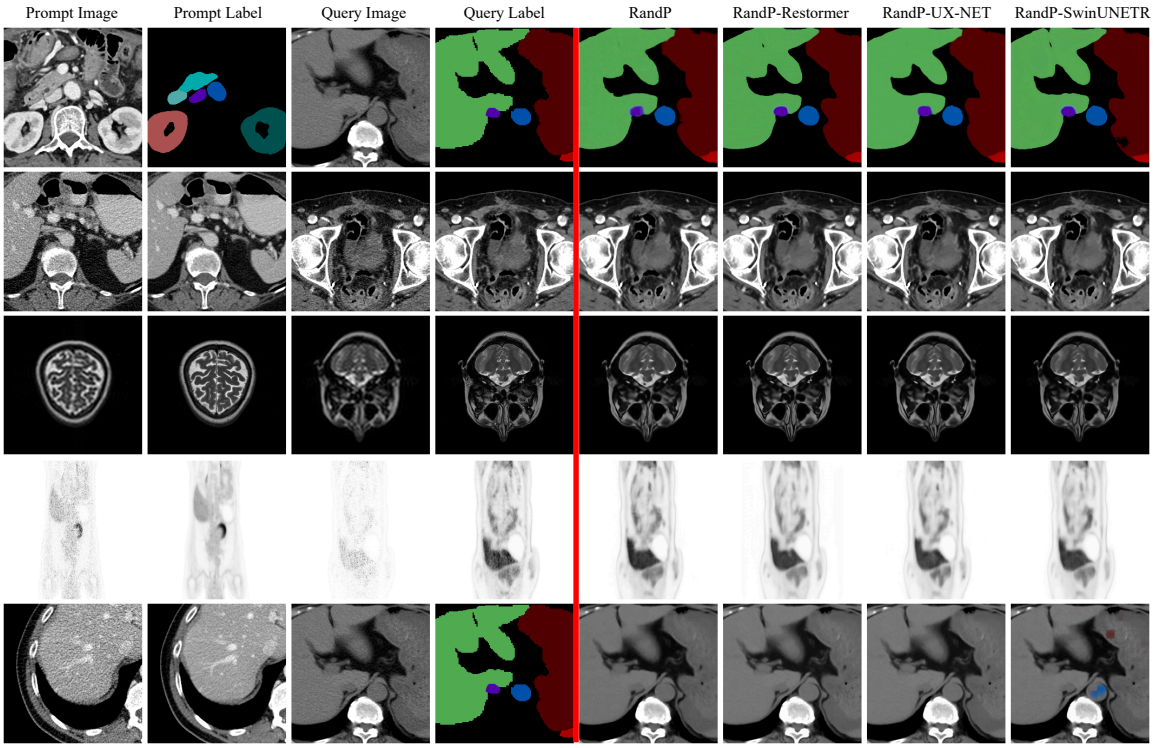

Figure 3: Qualitative evaluation of our RandP models.

Extending RandP to U-Net Variants. We extend the RandP framework to several widely-used U-Net variants in medical imaging. Specifically, we adopt pure advanced convolutional UX-Net (Lee et al., 2023), and SwinUNETR (Hatamizadeh et al., 2022), a window attention (Liu et al., 2021) based model. Both of them originally designed for 3D tasks, we adapt them to 2D settings. Additionally, we incorporate Restormer (Zamir et al., 2022), a modified-transformer-based model commonly used for low-level vision tasks. These combinations result in three RandP-based medical vICL models: RandP-UX-Net, RandP-SwinUNETR, and RandP-Restormer. We first train these models independently for each task. As shown in Table 3, in the single-task separate training setting, models with the same backbone generally show similar performance—for example, RandP and MVG (with ViT), and RandP-Restormer and AMIR (with Restormer) perform comparably. However, ViT-based models still lag behind task-specific U-Net-style architectures, particularly for the segmentation task.

We further perform joint multi-task training using the RandP framework across different backbones. As shown in Table 4, compared to single-task training, all backbones consistently benefit from joint optimization, demonstrating RandP's capability to mitigate inter-task conflicts during learning. However, the router-based AMIR framework shows a performance drop on the segmentation task under multi-task training compared to its single-task counterpart.

Both RandP-Restormer and AMIR use Restormer as the backbone. While AMIR introduces a complex task routing mechanism and incurs additional computational cost to reduce

Table 5: Ablation Study Results. Dice and SSIM are reported in percentage.

Models	Seg.	Denoising		Super-Resolution		PET synthesis	
	Dice	PSNR	SSIM	PSNR	SSIM	PSNR	SSIM
prompt-query token fusion strategies in ViT backbone							
Patch Merge	75.91	32.94	92.09	29.99	90.95	31.25	90.09
Greedy Matching	78.83	32.99	92.09	29.38	90.11	31.03	89.53
Hungarian Matching	**84.95**	**33.01**	**92.14**	**30.14**	**91.33**	**31.46**	**90.17**
Different Fusion Strategies when extending RandP to Restormer backbone							
First-Stage	84.71	33.97	92.89	30.74	92.31	31.44	90.38
Multi-Stage	83.62	33.97	92.78	**30.86**	92.47	31.13	90.12
Bottleneck	**85.70**	**33.99**	**92.92**	30.83	**92.50**	**32.08**	**91.04**

task interference, RandP-Restormer achieves clear and consistent improvements across all tasks, highlighting the effectiveness and efficiency of the RandP framework.

Fig. 3 shows the qualitative evaluation of our RandP models, the last row of it indicates that when we provide a denoising prompt for a segmentation query image, the model executes the task as instructed by the prompt, rather than simply memorizing the dataset.

Ablation Study 1: Query-Prompt Interaction strategy. Painter and MVG adopt apatch merging mechanism to fuse images and labels. However, as shown in Table 5, under the training-inference aligned masking strategy and the setting where the prompt label is not reconstructed, the performance of patch merging (i.e., spatially aligned visual tokens from the prompt image, prompt label, query image, and query label are summed at the merge layer) is significantly inferior to that of our proposed RandP Module. Another important aspect concerns the matching strategy between prompt tokens and query tokens during the fusion process. We experimented with both greedy matching and Hungarian matching. The primary difference lies in whether a single prompt token is allowed to match multiple query tokens. Experimental results show that Hungarian matching significantly outperforms greedy matching. We hypothesize that many-to-one matching leads to the neglect of numerous prompt tokens, thereby causing substantial prompt information loss.

Ablation Study 2: Fusion Strategy for Extending RandP to U-Net Variants. The mixed features from the **RandP** module are 16× downsampled relative to the input image. We explore three fusion strategies to integrate them into U-Net-style architectures:
1.First-stage fusion: Upsample the mixed features via pixel shuffle and concatenate with the input image at the first encoder stage.
2.Bottleneck fusion: Inject the mixed features directly into the bottleneck of the encoder.
3.Multi-stage fusion: Upsample the mixed features to multiple scales and add them to encoder features at corresponding stages.

Experiments show that bottleneck fusion achieves the best performance.

5. Conclusion

In this paper, we propose a medical vICL framework called RandP, which enables the execution of multiple different medical imaging tasks via visual prompt pairs. Our experiments demonstrate that RandP has superior performance while maintaining low computational cost. Furthermore, RandP can be extended to other architectures beyond ViT.

Acknowledgments

This work was supported by Natural Science Foundation of China under Grant 62271465, Suzhou Basic Research Program under Grant SYG202338, and Open Fund Project of Guangdong Academy of Medical Sciences, China (No. YKY-KF202206).

References

Yutong Bai, Xinyang Geng, Karttikeya Mangalam, Amir Bar, Alan L Yuille, Trevor Darrell, Jitendra Malik, and Alexei A Efros. Sequential modeling enables scalable learning for large vision models. In *Proceedings of the IEEE/CVF Conference on Computer Vision and Pattern Recognition*, pages 22861–22872, 2024.

Guha Balakrishnan, Amy Zhao, Mert R. Sabuncu, John Guttag, and Adrian V. Dalca. Voxelmorph: A learning framework for deformable medical image registration. *IEEE Transactions on Medical Imaging*, 38(8):1788–1800, August 2019. ISSN 1558-254X. doi: 10.1109/tmi.2019.2897538. URL http://dx.doi.org/10.1109/TMI.2019.2897538.

Amir Bar, Yossi Gandelsman, Trevor Darrell, Amir Globerson, and Alexei Efros. Visual prompting via image inpainting. *Advances in Neural Information Processing Systems*, 35: 25005–25017, 2022.

Daniel Bolya, Cheng-Yang Fu, Xiaoliang Dai, Peizhao Zhang, Christoph Feichtenhofer, and Judy Hoffman. Token merging: Your vit but faster, 2023. URL https://arxiv.org/abs/2210.09461.

Liang Chen, Haozhe Zhao, Tianyu Liu, Shuai Bai, Junyang Lin, Chang Zhou, and Baobao Chang. An image is worth 1/2 tokens after layer 2: Plug-and-play inference acceleration for large vision-language models, 2024. URL https://arxiv.org/abs/2403.06764.

Ruibo Chen, Tianyi Xiong, Yihan Wu, Guodong Liu, Zhengmian Hu, Lichang Chen, Yanshuo Chen, Chenxi Liu, and Heng Huang. Gpt-4 vision on medical image classification – a case study on covid-19 dataset, 2023. URL https://arxiv.org/abs/2310.18498.

Jia Deng, Wei Dong, Richard Socher, Li-Jia Li, Kai Li, and Li Fei-Fei. Imagenet: A large-scale hierarchical image database. In *Proceedings of the IEEE Conference on Computer Vision and Pattern Recognition (CVPR)*, pages 248–255, 2009.

Lee R Dice. Measures of the amount of ecologic association between species. *Ecology*, 26 (3):297–302, 1945.

Patrick Esser, Robin Rombach, and Bjorn Ommer. Taming transformers for high-resolution image synthesis. In *Proceedings of the IEEE/CVF conference on computer vision and pattern recognition*, pages 12873–12883, 2021.

Dyke Ferber, Georg Wölflein, Isabella C Wiest, Marta Ligero, Srividhya Sainath, Narmin Ghaffari Laleh, Omar SM El Nahhas, Gustav Müller-Franzes, Dirk Jäger, Daniel Truhn, et al. In-context learning enables multimodal large language models to classify cancer pathology images. *Nature Communications*, 15(1):10104, 2024.

Ross Girshick. Fast r-cnn, 2015. URL https://arxiv.org/abs/1504.08083.

Ali Hatamizadeh, Vishwesh Nath, Yucheng Tang, Dong Yang, Holger Roth, and Daguang Xu. Swin unetr: Swin transformers for semantic segmentation of brain tumors in mri images, 2022. URL https://arxiv.org/abs/2201.01266.

Kaiming He, Xinlei Chen, Saining Xie, Yanghao Li, Piotr Dollár, and Ross Girshick. Masked autoencoders are scalable vision learners. In *Proceedings of the IEEE/CVF conference on computer vision and pattern recognition*, pages 16000–16009, 2022.

Yuanfeng Ji, Haotian Bai, Chongjian Ge, Jie Yang, Ye Zhu, Ruimao Zhang, Zhen Li, Lingyan Zhanng, Wanling Ma, Xiang Wan, et al. Amos: A large-scale abdominal multi-organ benchmark for versatile medical image segmentation. *Advances in neural information processing systems*, 35:36722–36732, 2022.

Menglin Jia, Luming Tang, Bor-Chun Chen, Claire Cardie, Serge Belongie, Bharath Hariharan, and Ser-Nam Lim. Visual prompt tuning. In *European conference on computer vision*, pages 709–727. Springer, 2022.

Harold W Kuhn. The hungarian method for the assignment problem. *Naval research logistics quarterly*, 2(1-2):83–97, 1955.

Bennett Landman, Zhoubing Xu, J Igelsias, Martin Styner, T Langerak, and Arno Klein. Miccai multi-atlas labeling beyond the cranial vault–workshop and challenge. In *Proc. MICCAI Multi-Atlas Labeling Beyond Cranial Vault—Workshop Challenge*, volume 5, page 12, 2015.

Ho Hin Lee, Shunxing Bao, Yuankai Huo, and Bennett A. Landman. 3d ux-net: A large kernel volumetric convnet modernizing hierarchical transformer for medical image segmentation, 2023. URL https://arxiv.org/abs/2209.15076.

Han Li, Long Chen, Hu Han, and S Kevin Zhou. Satr: Slice attention with transformer for universal lesion detection. In *International conference on medical image computing and computer-assisted intervention*, pages 163–174. Springer, 2022a.

Yanghao Li, Hanzi Mao, Ross Girshick, and Kaiming He. Exploring plain vision transformer backbones for object detection. In *European conference on computer vision*, pages 280–296. Springer, 2022b.

Geert Litjens, Robert Toth, Wendy J. M. van de Ven, Caroline M. A. Hoeks, Sjoerd Kerkstra, Bram van Ginneken, Graham Vincent, Gwenael Guillard, Neil Birbeck, Jindang Zhang, Robin Strand, Filip Malmberg, Yangming Ou, Christos Davatzikos, Matthias Kirschner, Florian Jung, Jing Yuan, Wu Qiu, Qinquan Gao, Philip E. Edwards, Bianca Maan, Ferdinand van der Heijden, Soumya Ghose, Jhimli Mitra, Jason Dowling, Dean Barratt, Henkjan Huisman, and Anant Madabhushi. Evaluation of prostate segmentation algorithms for mri: The promise12 challenge. *Medical Image Analysis*, 18(2):359–373, 2014.

Yihao Liu, Xiangyu Chen, Xianzheng Ma, Xintao Wang, Jiantao Zhou, Yu Qiao, and Chao Dong. Unifying image processing as visual prompting question answering, 2024. URL https://arxiv.org/abs/2310.10513.

Ze Liu, Yutong Lin, Yue Cao, Han Hu, Yixuan Wei, Zheng Zhang, Stephen Lin, and Baining Guo. Swin transformer: Hierarchical vision transformer using shifted windows. In *Proceedings of the IEEE/CVF international conference on computer vision*, pages 10012–10022, 2021.

M. LLC. Ixi dataset. https://brain-development.org/ixi-dataset/, 2024. accessed: 2024-01-15.

Cynthia H McCollough, Adam C Bartley, Rickey E Carter, Baiyu Chen, Tammy A Drees, Phillip Edwards, David R Holmes III, Alice E Huang, Farhana Khan, Shuai Leng, et al. Low-dose ct for the detection and classification of metastatic liver lesions: results of the 2016 low dose ct grand challenge. *Medical physics*, 44(10):e339–e352, 2017.

OpenAI, Josh Achiam, Steven Adler, Sandhini Agarwal, Lama Ahmad, Ilge Akkaya, Florencia Leoni Aleman, Diogo Almeida, Janko Altenschmidt, Sam Altman, Shyamal Anadkat, Red Avila, Igor Babuschkin, Suchir Balaji, Valerie Balcom, Paul Baltescu, Haiming Bao, Mohammad Bavarian, Jeff Belgum, Irwan Bello, Jake Berdine, Gabriel Bernadett-Shapiro, Christopher Berner, Lenny Bogdonoff, Oleg Boiko, Madelaine Boyd, Anna-Luisa Brakman, Greg Brockman, Tim Brooks, Miles Brundage, Kevin Button, Trevor Cai, Rosie Campbell, Andrew Cann, Brittany Carey, Chelsea Carlson, Rory Carmichael, Brooke Chan, Che Chang, Fotis Chantzis, Derek Chen, Sully Chen, Ruby Chen, Jason Chen, Mark Chen, Ben Chess, Chester Cho, Casey Chu, Hyung Won Chung, Dave Cummings, Jeremiah Currier, Yunxing Dai, Cory Decareaux, Thomas Degry, Noah Deutsch, Damien Deville, Arka Dhar, David Dohan, Steve Dowling, Sheila Dunning, Adrien Ecoffet, Atty Eleti, Tyna Eloundou, David Farhi, Liam Fedus, Niko Felix, Simón Posada Fishman, Juston Forte, Isabella Fulford, Leo Gao, Elie Georges, Christian Gibson, Vik Goel, Tarun Gogineni, Gabriel Goh, Rapha Gontijo-Lopes, Jonathan Gordon, Morgan Grafstein, Scott Gray, Ryan Greene, Joshua Gross, Shixiang Shane Gu, Yufei Guo, Chris Hallacy, Jesse Han, Jeff Harris, Yuchen He, Mike Heaton, Johannes Heidecke, Chris Hesse, Alan Hickey, Wade Hickey, Peter Hoeschele, Brandon Houghton, Kenny Hsu, Shengli Hu, Xin Hu, Joost Huizinga, Shantanu Jain, Shawn Jain, Joanne Jang, Angela Jiang, Roger Jiang, Haozhun Jin, Denny Jin, Shino Jomoto, Billie Jonn, Heewoo Jun, Tomer Kaftan, Łukasz Kaiser, Ali Kamali, Ingmar Kanitscheider, Nitish Shirish Keskar, Tabarak Khan, Logan Kilpatrick, Jong Wook Kim, Christina Kim, Yongjik Kim, Jan Hendrik Kirchner, Jamie Kiros, Matt Knight, Daniel Kokotajlo, Łukasz Kondraciuk, Andrew Kondrich, Aris Konstantinidis, Kyle Kosic, Gretchen Krueger, Vishal Kuo, Michael Lampe, Ikai Lan, Teddy Lee, Jan Leike, Jade Leung, Daniel Levy, Chak Ming Li, Rachel Lim, Molly Lin, Stephanie Lin, Mateusz Litwin, Theresa Lopez, Ryan Lowe, Patricia Lue, Anna Makanju, Kim Malfacini, Sam Manning, Todor Markov, Yaniv Markovski, Bianca Martin, Katie Mayer, Andrew Mayne, Bob McGrew, Scott Mayer McKinney, Christine McLeavey, Paul McMillan, Jake McNeil, David Medina, Aalok Mehta, Jacob Menick, Luke Metz, Andrey Mishchenko, Pamela Mishkin, Vinnie Monaco, Evan Morikawa, Daniel Mossing, Tong Mu, Mira Murati, Oleg Murk, David Mély, Ashvin Nair, Reiichiro Nakano, Rajeev Nayak,

Arvind Neelakantan, Richard Ngo, Hyeonwoo Noh, Long Ouyang, Cullen O'Keefe, Jakub Pachocki, Alex Paino, Joe Palermo, Ashley Pantuliano, Giambattista Parascandolo, Joel Parish, Emy Parparita, Alex Passos, Mikhail Pavlov, Andrew Peng, Adam Perelman, Filipe de Avila Belbute Peres, Michael Petrov, Henrique Ponde de Oliveira Pinto, Michael, Pokorny, Michelle Pokrass, Vitchyr H. Pong, Tolly Powell, Alethea Power, Boris Power, Elizabeth Proehl, Raul Puri, Alec Radford, Jack Rae, Aditya Ramesh, Cameron Raymond, Francis Real, Kendra Rimbach, Carl Ross, Bob Rotsted, Henri Roussez, Nick Ryder, Mario Saltarelli, Ted Sanders, Shibani Santurkar, Girish Sastry, Heather Schmidt, David Schnurr, John Schulman, Daniel Selsam, Kyla Sheppard, Toki Sherbakov, Jessica Shieh, Sarah Shoker, Pranav Shyam, Szymon Sidor, Eric Sigler, Maddie Simens, Jordan Sitkin, Katarina Slama, Ian Sohl, Benjamin Sokolowsky, Yang Song, Natalie Staudacher, Felipe Petroski Such, Natalie Summers, Ilya Sutskever, Jie Tang, Nikolas Tezak, Madeleine B. Thompson, Phil Tillet, Amin Tootoonchian, Elizabeth Tseng, Preston Tuggle, Nick Turley, Jerry Tworek, Juan Felipe Cerón Uribe, Andrea Vallone, Arun Vijayvergiya, Chelsea Voss, Carroll Wainwright, Justin Jay Wang, Alvin Wang, Ben Wang, Jonathan Ward, Jason Wei, CJ Weinmann, Akila Welihinda, Peter Welinder, Jiayi Weng, Lilian Weng, Matt Wiethoff, Dave Willner, Clemens Winter, Samuel Wolrich, Hannah Wong, Lauren Workman, Sherwin Wu, Jeff Wu, Michael Wu, Kai Xiao, Tao Xu, Sarah Yoo, Kevin Yu, Qiming Yuan, Wojciech Zaremba, Rowan Zellers, Chong Zhang, Marvin Zhang, Shengjia Zhao, Tianhao Zheng, Juntang Zhuang, William Zhuk, and Barret Zoph. Gpt-4 technical report, 2024. URL https://arxiv.org/abs/2303.08774.

Sucheng Ren, Xiaoke Huang, Xianhang Li, Junfei Xiao, Jieru Mei, Zeyu Wang, Alan Yuille, and Yuyin Zhou. Medical vision generalist: Unifying medical imaging tasks in context, 2024. URL https://arxiv.org/abs/2406.05565.

Olaf Ronneberger, Philipp Fischer, and Thomas Brox. U-net: Convolutional networks for biomedical image segmentation. In *Medical image computing and computer-assisted intervention–MICCAI 2015: 18th international conference, Munich, Germany, October 5-9, 2015, proceedings, part III 18*, pages 234–241. Springer, 2015.

Yanpeng Sun, Qiang Chen, Jian Wang, Jingdong Wang, and Zechao Li. Exploring effective factors for improving visual in-context learning. *IEEE Transactions on Image Processing*, 2025.

Wei Suo, Lanqing Lai, Mengyang Sun, Hanwang Zhang, Peng Wang, and Yanning Zhang. Visual prompt selection for in-context learning segmentation, 2024. URL https://arxiv.org/abs/2407.10233.

Keyu Tian, Yi Jiang, Qishuai Diao, Chen Lin, Liwei Wang, and Zehuan Yuan. Designing bert for convolutional networks: Sparse and hierarchical masked modeling, 2023. URL https://arxiv.org/abs/2301.03580.

Ashish Vaswani, Noam Shazeer, Niki Parmar, Jakob Uszkoreit, Llion Jones, Aidan N. Gomez, Lukasz Kaiser, and Illia Polosukhin. Attention is all you need, 2023. URL https://arxiv.org/abs/1706.03762.

Ge Wang, Yi Zhang, Xiaojing Ye, and Xuanqin Mou. *Machine learning for tomographic imaging*. IOP Publishing, 2019.

Xinlong Wang, Wen Wang, Yue Cao, Chunhua Shen, and Tiejun Huang. Images speak in images: A generalist painter for in-context visual learning. In *Proceedings of the IEEE/CVF Conference on Computer Vision and Pattern Recognition*, pages 6830–6839, 2023.

Zhou Wang, Alan C Bovik, Hamid R Sheikh, and Eero P Simoncelli. Image quality assessment: from error visibility to structural similarity. *IEEE transactions on image processing*, 13(4):600–612, 2004.

Zichen Wen, Yifeng Gao, Shaobo Wang, Junyuan Zhang, Qintong Zhang, Weijia Li, Conghui He, and Linfeng Zhang. Stop looking for important tokens in multimodal language models: Duplication matters more, 2025. URL https://arxiv.org/abs/2502.11494.

Chaoyi Wu, Jiayu Lei, Qiaoyu Zheng, Weike Zhao, Weixiong Lin, Xiaoman Zhang, Xiao Zhou, Ziheng Zhao, Ya Zhang, Yanfeng Wang, and Weidi Xie. Can gpt-4v(ision) serve medical applications? case studies on gpt-4v for multimodal medical diagnosis, 2023. URL https://arxiv.org/abs/2310.09909.

Xian Wu, Shuxin Yang, Zhaopeng Qiu, Shen Ge, Yangtian Yan, Xingwang Wu, Yefeng Zheng, S. Kevin Zhou, and Li Xiao. Deltanet:conditional medical report generation for covid-19 diagnosis, 2022. URL https://arxiv.org/abs/2211.13229.

Zhenda Xie, Zheng Zhang, Yue Cao, Yutong Lin, Jianmin Bao, Zhuliang Yao, Qi Dai, and Han Hu. Simmim: A simple framework for masked image modeling. In *Proceedings of the IEEE/CVF conference on computer vision and pattern recognition*, pages 9653–9663, 2022.

Zhiwen Yang, Haowei Chen, Ziniu Qian, Yang Yi, Hui Zhang, Dan Zhao, Bingzheng Wei, and Yan Xu. All-in-one medical image restoration via task-adaptive routing. In *International Conference on Medical Image Computing and Computer-Assisted Intervention*, pages 67–77. Springer, 2024.

Jin Ye, Junlong Cheng, Jianpin Chen, Zhongying Deng, Tianbin Li, Haoyu Wang, Yanzhou Su, Ziyan Huang, Jilong Chen, Lei Jiang, Hui Sun, Min Zhu, Shaoting Zhang, Junjun He, and Yu Qiao. Sa-med2d-20m dataset: Segment anything in 2d medical imaging with 20 million masks, 2023. URL https://arxiv.org/abs/2311.11969.

Yubiao Yue and Zhenzhang Li. Medmamba: Vision mamba for medical image classification, 2024. URL https://arxiv.org/abs/2403.03849.

Syed Waqas Zamir, Aditya Arora, Salman Khan, Munawar Hayat, Fahad Shahbaz Khan, and Ming-Hsuan Yang. Restormer: Efficient transformer for high-resolution image restoration. In *Proceedings of the IEEE/CVF conference on computer vision and pattern recognition*, pages 5728–5739, 2022.

Jiahao Zhang, Bowen Wang, Liangzhi Li, Yuta Nakashima, and Hajime Nagahara. Instruct me more! random prompting for visual in-context learning. In *Proceedings of the IEEE/CVF Winter Conference on Applications of Computer Vision*, pages 2597–2606, 2024.

Jiahao Zhang, Bowen Wang, Hong Liu, Liangzhi Li, Yuta Nakashima, and Hajime Nagahara. E-inmemo: Enhanced prompting for visual in-context learning. *Journal of Imaging*, 11(7):232, 2025a.

Qizhe Zhang, Aosong Cheng, Ming Lu, Renrui Zhang, Zhiyong Zhuo, Jiajun Cao, Shaobo Guo, Qi She, and Shanghang Zhang. Beyond text-visual attention: Exploiting visual cues for effective token pruning in vlms, 2025b. URL https://arxiv.org/abs/2412.01818.

Yuanhan Zhang, Kaiyang Zhou, and Ziwei Liu. What makes good examples for visual in-context learning? *Advances in Neural Information Processing Systems*, 36:17773–17794, 2023.

S Kevin Zhou, Hayit Greenspan, Christos Davatzikos, James S Duncan, Bram Van Ginneken, Anant Madabhushi, Jerry L Prince, Daniel Rueckert, and Ronald M Summers. A review of deep learning in medical imaging: Imaging traits, technology trends, case studies with progress highlights, and future promises. *Proceedings of the IEEE*, 109(5): 820–838, 2021.

Yucheng Zhou, Xiang Li, Qianning Wang, and Jianbing Shen. Visual in-context learning for large vision-language models, 2024. URL https://arxiv.org/abs/2402.11574.

Appendix A. Pseudocode of RandP

Algorithm 1 Retrieval and Propagate for Prompt-Query Interaction

Input: Prompt image $\mathbf{I}_{pi}$, Prompt label $\mathbf{I}_{pl}$, Query image $\mathbf{I}_{qi}$
Output: Prompt-Query Fusion Feature $\mathbf{X}$
Step 1: Patch Embedding
$\mathbf{Z}_{pi},\ \mathbf{Z}_{pl},\ \mathbf{Z}_{qi} \leftarrow \text{PatchEmbed}(\mathbf{I}_{pi},\ \mathbf{I}_{pl},\ \mathbf{I}_{qi}) + \mathbf{P}$
Step 2: Shallow ViT for Feature Extraction
$\mathbf{X}_{pi},\ \mathbf{X}_{pl},\ \mathbf{X}_{qi},\ \mathbf{X}_{ql} \leftarrow \text{ViT}([\mathbf{Z}_{pi},\ \mathbf{Z}_{pl},\ \mathbf{Z}_{qi},\ [\text{MASK}]])$
Step 3: Cosine Similarity Matching
$\mathbf{S} \leftarrow \text{Norm}(\mathbf{X}_{pi}) \cdot \text{Norm}(\mathbf{X}_{qi})^{\top}$
$\mathcal{M} \leftarrow \text{Hungarian}(-\mathbf{S})$
Step 4: Reorder Prompt Tokens
$\mathcal{M}(\mathbf{X}_{pi}) \leftarrow \text{Reorder}(\mathbf{X}_{pi}, \mathcal{M})$
$\mathcal{M}(\mathbf{X}_{pl}) \leftarrow \text{Reorder}(\mathbf{X}_{pl}, \mathcal{M})$
Step 5: Prompt-Query Token Fusion
$\mathbf{X} \leftarrow \text{Linear}(\text{Concat}[\mathcal{M}(\mathbf{X}_{pi}),\ \mathcal{M}(\mathbf{X}_{pl}),\ \mathbf{X}_{qi},\ \mathbf{X}_{ql}])$
Return X

Appendix B. Prompt Analysis

Numerous studies (Bar et al., 2022; Sun et al., 2025; Zhang et al., 2023) have highlighted the sensitivity of vICL models to the choice of prompts. Some works have explored heuristic strategies (Sun et al., 2025; Zhang et al., 2023; Suo et al., 2024) for selecting optimal visual prompts, while others have investigated learning-based approaches (Jia et al., 2022; Zhang et al., 2024, 2025a) to prompt construction. Given the high demand for controllability in medical image analysis, vICL models are designed to take both the query image and a prompt pair—consisting of an image and its corresponding label—as input. Therefore, we conduct a comprehensive analysis of the prompt component in trained visual ICL models.

Table 6: Average standard deviation of the performance of trained medical vICL models across 20 different prompts.

	Segmentation Dice-std	**Denoising**	**Super-Resolution** PSNR-std	**PET synthesis**
MVG	**0.00455**	0.00880	**0.0057**	0.0353
RandP	0.00704	0.00695	0.0069	0.0416
RandP-UX-NET	0.00855	0.00526	0.0195	0.0327
RandP-SwinUNETR	0.00968	0.00815	0.0272	**0.0284**
RandP-Restormer	0.00722	**0.00475**	0.0239	0.0336

Standard Deviations Across Different Prompt Pairs. First, for each query image in the test set, 20 prompt pairs from the same task were randomly selected for inference. We then calculated the standard deviation of performance metrics across these inferences. Finally, we averaged these standard deviations over the entire test set. The results are summarized in Table 6.

When using ViT as the backbone, our RandP model exhibits higher standard deviations in segmentation, super-resolution, and PET synthesis compared to MVG. We attribute this to our more aggressive merging strategy between prompt tokens and query tokens. When extending the RandP framework to other U-Net variants, the standard deviation tends to increase further across most tasks relative to the ViT-based version.

However, a lower standard deviation is not always preferable. We argue that a moderately low standard deviation is desirable—it ensures model stability across prompts while allowing prompts to exert meaningful influence on the model's interpretation of the query. The results suggest that our trained medical visual ICL models under the RandP framework maintain appropriately low standard deviations, ensuring stable performance under different prompts. Meanwhile, the variability in prompt effectiveness implies that some prompts are better than others. Identifying optimal prompts for medical visual ICL models will be an important direction for our future work.

Table 7: Performance difference between learned prompts and random prompts.

	Segmentation	**Denoising**		**Super-Resolution**		**PET synthesis**	
	Dice	PSNR	SSIM	PSNR	SSIM	PSNR	SSIM
Random Prompts	84.95	33.01	92.14	**30.14**	**91.33**	**31.46**	**90.17**
Learned Prompts	**85.11**	**33.04**	**92.16**	30.12	91.32	31.39	90.16

Learned Prompt vs. Random Prompt In addition, we froze the parameters of the trained visual ICL model and treated the prompt image and prompt label as learnable embeddings. Each task was associated with a distinct set of prompt embeddings, enabling task-specific adaptation without modifying the backbone. These learnable embeddings are optimized using a learning rate of 1e-4 for 10 epochs without any warm-up schedule. During inference, we used the corresponding learned prompt embeddings for each task. As shown in Table 7, due to the marginal performance gap between learned and random prompts, the use of learned prompts can be seen to enhance the stability of medical visual ICL models. The results are presented in Table 7, we observe that the performance difference between the learned prompts and randomly selected prompts is marginal. These results indicate that learned prompts further enhance the stability of medical visual ICL models. Upon visualizing the learned prompts, we find that they do not resemble semantically meaningful images; rather, they appear as structured noise patterns with no obvious visual interpretation.